

Article

Flexible Co(II)-and Ni(II)-Based Cationic 2D Metal–Organic Frameworks Based on a Charge-Neutral (O,O)-Donor Bridge

Pavel A. Demakov , Konstantin A. Kovalenko , Alexander N. Lavrov and Vladimir P. Fedin 

Nikolaev Institute of Inorganic Chemistry, Siberian Branch of the Russian Academy of Sciences, Novosibirsk 630090, Russia; k.a.kovalenko@niic.nsc.ru (K.A.K.); lavrov@niic.nsc.ru (A.N.L.)

* Correspondence: demakov@niic.nsc.ru (P.A.D.); cluster@niic.nsc.ru (V.P.F.)

Abstract: Two new metal–organic frameworks based on highly flexible 1,4-diazabicyclo[2.2.2]octane N,N'-dioxide (odabco) ligands were successfully synthesized and characterized. Their crystallographic formulae are $[M(\text{DMF})_2(\text{odabco})_2](\text{ClO}_4)_2 \cdot \text{dioxane}$, where $M^{2+} = \text{Co}^{2+}$ (**1**) and Ni^{2+} (**2**), and DMF is N,N-dimethylformamide. The title compounds possess cationic 2D coordination networks filled with perchlorate anions and dioxane solvent molecules in the interlayer space, with 20% solvent accessible volume. Carbon dioxide adsorption measurements for desolvated samples **1a** and **2a** gave $511 \text{ m}^2/\text{g}$ and $377 \text{ m}^2/\text{g}$ specific surface areas, respectively, revealing the first example of gas adsorption properties in the structure based on a flexible odabco bridge, despite the presence of large counteranions within the positively charged network. Magnetization measurements for **1**, **1a**, **2** and **2a** reveal their paramagnetic nature to be in a reasonable agreement with crystal structures, and almost no solvent dependence of the magnetization characteristics. A decrease in the effective magnetic moment observed at low temperatures is attributed mostly to zero-field level-splitting in the octahedral Ni^{2+} and Co^{2+} ions.

Keywords: metal–organic framework; coordination polymer; cationic networks; aliphatic ligands; gas adsorption; magnetic properties; diffuse reflectance spectroscopy



Citation: Demakov, P.A.; Kovalenko, K.A.; Lavrov, A.N.; Fedin, V.P. Flexible Co(II)-and Ni(II)-Based Cationic 2D Metal–Organic Frameworks Based on a Charge-Neutral (O,O)-Donor Bridge. *Inorganics* **2023**, *11*, 259. <https://doi.org/10.3390/inorganics11060259>

Academic Editors: Wolfgang Linert, Koichiro Takao, Gabriel García Sánchez and David Turner

Received: 22 May 2023
Revised: 13 June 2023
Accepted: 15 June 2023
Published: 17 June 2023



Copyright: © 2023 by the authors. Licensee MDPI, Basel, Switzerland. This article is an open access article distributed under the terms and conditions of the Creative Commons Attribution (CC BY) license (<https://creativecommons.org/licenses/by/4.0/>).

1. Introduction

Metal–organic frameworks (MOFs) represent an extensively growing class of coordination compounds, consisting of metal blocks and organic bridging ligands. Typically, MOFs are based on carboxylate anions, capable of a decently strong binding to the wide range of metal ions [1,2], or di-/polytopic N-donor bridges, whose strong coordination abilities are mostly related to Pearson's soft cations [3–5]. Metal–organic frameworks based on ligands of such types as well as their-derived composites are widely used in the selective adsorption [6], gas separations [7], electrochemical devices [8,9] and single-molecule magnets [10].

Electroneutrality is a rather rare feature of polytopic (O,O)-donor bridges in polymeric coordination networks. Such uncharged bridging ligand classes as polyethers [11], carbohydrates [12,13], cyclodextrins [14,15], and different type polyamides [16,17], including cucurbit[n]urils [18], are mainly represented by alkali and alkaline earth metal-based cationic networks in MOF chemistry, with an accordingly limited range of functional properties.

At the same time, positively charged coordination frameworks are promising for the synthesis of highly crystalline anion sorbents [19–22], sensors [22–24], and for easy post-synthetic functionalization via ion exchange [25–29]. Using charge-neutral (O,O)-donors with wide coordination abilities is a powerful route for the design of cationic MOFs. Aromatic N,N'-dioxides are apparently the most studied subclass of uncharged (O,O)-donors in this chemistry. Such types of ligands can form strong coordination bonds with Pearson's both hard and soft cations due to a high negative charge located on N-oxide

oxygen atoms [30]. Incorporation of large functional anions, such as POMs [31], cyanometallates [32,33], halometallates [34,35], and borane clusters [36], has been achieved for aromatic N,N'-dioxide-based MOFs, and their guest-dependent structural dynamics [37], thermochromism [38], multibanded luminescence [30,39,40], photovoltaic generation [34,35], and slow magnetic relaxation [41] have been extensively studied in previous works.

On the contrary, aliphatic N,N'-dioxides are poorly studied as ligands in MOF chemistry. 1,4-Diazabicyclo[2.2.2]octane N,N'-dioxide (odabco) is easily synthesized from the corresponding tertiary amine dabco [42]. Previous studies have revealed that odabco does not suffer from steric hindrance [43], being able to hexa-coordinate different transition metal ions [44–47] in spite of its bulky alicyclic core. Further, the odabco alicyclic bridge possesses a very high degree of flexibility due to its several inversion, rotation and torsion modes, resulting in very high structural diversity [45,48,49], possible breathing, and ferroelectricity [50–52] in the relevant structures. Expanding the family of alicyclic N,N'-dioxide-based MOFs towards magnetic and catalytically active transition metal ions, such as Co(II) and Ni(II), could result in new types of functional and dynamic materials. So far, only two cobalt- [46] and no nickel-based odabco structures have been reported, to the best of our knowledge. Herein, we report the synthesis, crystal structures, and characterization of two new metal–organic frameworks with the formulae $[M(\text{DMF})_2(\text{odabco})_2](\text{ClO}_4)_2 \cdot \text{dioxane}$, where $M^{2+} = \text{Co}^{2+}$ (**1**) and Ni^{2+} (**2**), DMF = N,N-dimethylformamide. Isostructural **1** and **2** possess positively charged layered coordination networks with the interlayer space filled by large perchlorate counteranions and solvent molecules. The permanent porosity of the activated samples **1a** and **2a** was confirmed by CO₂ adsorption measurements. Magnetization measurements revealed the purely paramagnetic properties of the studied compounds, in agreement with the large spatial separation between the metal ions in their crystal structures.

2. Results and Discussion

2.1. Synthesis and Characterization

A porous metal–organic framework with the crystallographic formula $[\text{Co}(\text{DMF})_2(\text{odabco})_2](\text{ClO}_4)_2 \cdot \text{dioxane}$ (**1**) was obtained by heating cobalt(II) perchlorate and odabco·3H₂O₂ in a mixture of N,N-dimethylformamide (DMF) and dioxane, acidified by HClO₄, at 90 °C for two days. Lowering the content of perchloric acid in a synthetic system leads to the formation of visually observable black or brown impurities, while increasing the HClO₄ content reduces the yield. Similar pink plate-like crystals form if using pure DMF instead of a DMF/dioxane mixture, but the addition of dioxane was found to improve the diffraction, forming very thin plates, and to lower their twinning degree. Compound $[\text{Ni}(\text{DMF})_2(\text{odabco})_2](\text{ClO}_4)_2 \cdot \text{dioxane}$ (**2**) was synthesized using a similar method, except changing cobalt(II) perchlorate to nickel(II) perchlorate. Powder X-ray diffraction (PXRD) data for the filtered samples confirm their phase purity, although a pronounced preferred orientation of thin plates apparently exists according to the obtained patterns (Figure A1; see Appendix A). Elemental CHNCl analysis data (see the experimental) for the bulk sample of **1** correspond well to the formula $[\text{Co}(\text{DMF})_2(\text{odabco})_2](\text{ClO}_4)_2 \cdot 0.3\text{dioxane} \cdot 3\text{H}_2\text{O}$, which appears in a reasonable agreement with its coordination network composition and porosity, showing some substitution of guest dioxane by water in the sample during its storage. The CHNCl analysis data for **2** almost perfectly match its crystallographic formula $[\text{Ni}(\text{DMF})_2(\text{odabco})_2](\text{ClO}_4)_2 \cdot \text{dioxane}$, also confirming both the chemical nature and purity of the title compound.

2.2. Crystal Structure Description

According to single-crystal X-ray diffraction (SCXRD) data, compounds **1** and **2** are isostructural. Therefore, only crystal structure of cobalt(II)-based **1** will be described in detail. The compound crystallizes in the monoclinic system with a C2/c space group. The independent unit consists of half of a Co(II) ion, one odabco and one DMF ligand, one perchlorate counteranion, and a half of a dioxane molecule. Each Co(II) is coordinated

by four O atoms of four odabco bridges and two O atoms of two DMF terminal ligands (Figure 1a), thus adopting an octahedral environment. The Co–O(odabco) bond lengths are 2.040(2) Å and 2.1238(18) Å. These values fit well to the typical bond lengths' range for octahedral Co(II) complexes with different N-oxides, nitroxyl radicals, and oxime ligands [53–60]. The Co–O(DMF) bond length is 2.156(2) Å. Due to the opposite location of two terminal DMF ligands, Co(II) ions represent square nodes, which are interconnected in four directions with extended N,N'-dioxide bridges to form a rectangular *sql*-type layer (Figure 1b). The layer windows are ca. 3.3 Å² in size. However, neighboring layers are packed in an ABAB manner to each other, with a 0.5*a* + 0.5*c* offset; thus, no channel is formed in the 3D structure of **1** by their windows.

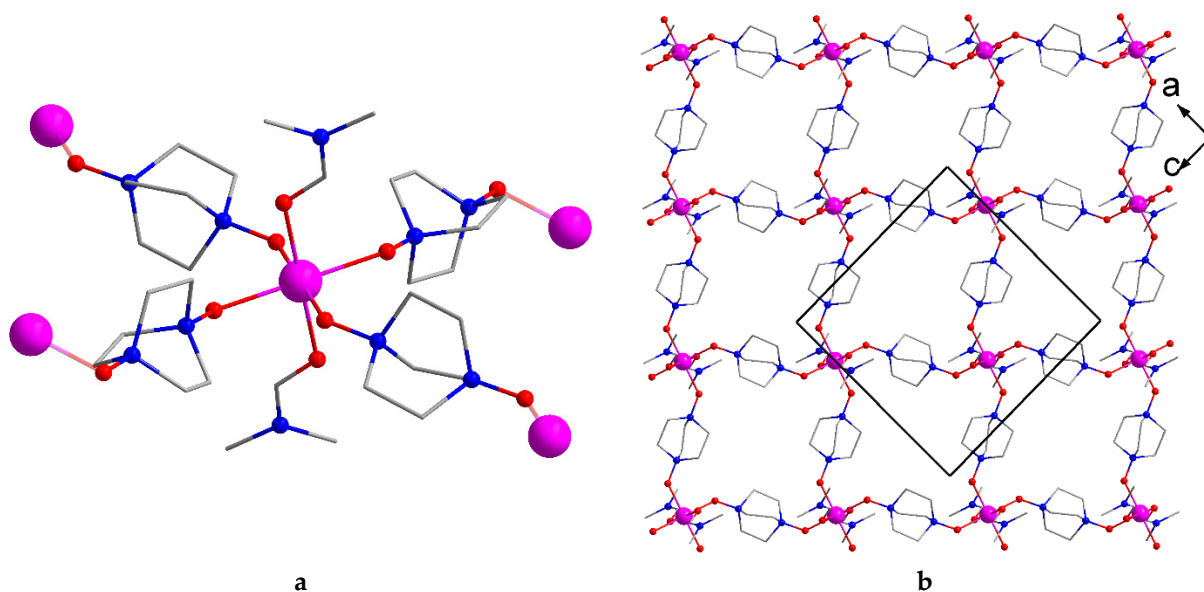


Figure 1. Co(II) coordination environment (a) and view of the $\{Co(DMF)_2(odabco)_2\}_n^{2n+}$ coordination layer along the *b* axis (b) in **1**. Co atoms are purple, O atoms are red, N atoms are blue. H atoms and guest moieties are not shown. The black rectangle in Figure 1b shows a projection of *a* and *c* unit cell edges.

The interlayer space contains other channels of ca. 2.5 Å² size, paved by coordinated DMF and odabco moieties in the perpendicular directions (Figure 2a). Guest dioxane molecules, which are disordered over two close positions, are located in the center of the channels, while perchlorates are situated nearer the abovementioned intralayer windows (Figure 2b). An analysis of the closest molecular environment of perchlorate reveals several weak C–H . . . O hydrogen bonds to the aliphatic core of odabco bridges and the DMF methyl groups, the latter being the shortest ones. The O(ClO₄) . . . C(CH₃) distances are 3.13 Å and 3.19 Å, slightly lower than the sum of (C+O) WdW radii (ca. 3.22 Å). The corresponding CHO angles are slightly bent to 150° and 140°, respectively, suggesting hydrogen bonding. The O(ClO₄) . . . C(CH₂) distances, also marked in Figure 3b, lie in the 3.32 . . . 3.42 Å range and possess bending angles of 138 . . . 167°, also fitting to the criterion of weak C–H . . . O hydrogen bonds (less than 3.5 Å C . . . O distance and more than 120° CHO angle), previously formulated in the relevant literature [61]. At the same time, each Co . . . O(ClO₄) distance exceeds 5.7 Å, showing that the exact location of poorly coordinating perchlorate is only driven by weak intermolecular interactions between the anion and aliphatic moieties of the coordination framework. Such cationic behavior is typically achieved for Co(II) and Ni(II)-based polymeric complexes containing perchlorates, if using diverse types of charge-neutral bridging ligands [62–66]. Examples of Co(II) and Ni(II) perchlorates with anionic bridges are much rarer [67,68]. A few works also report the coordination of perchlorate with Co(II) or Ni(II) within the relevant polymeric networks [69,70].

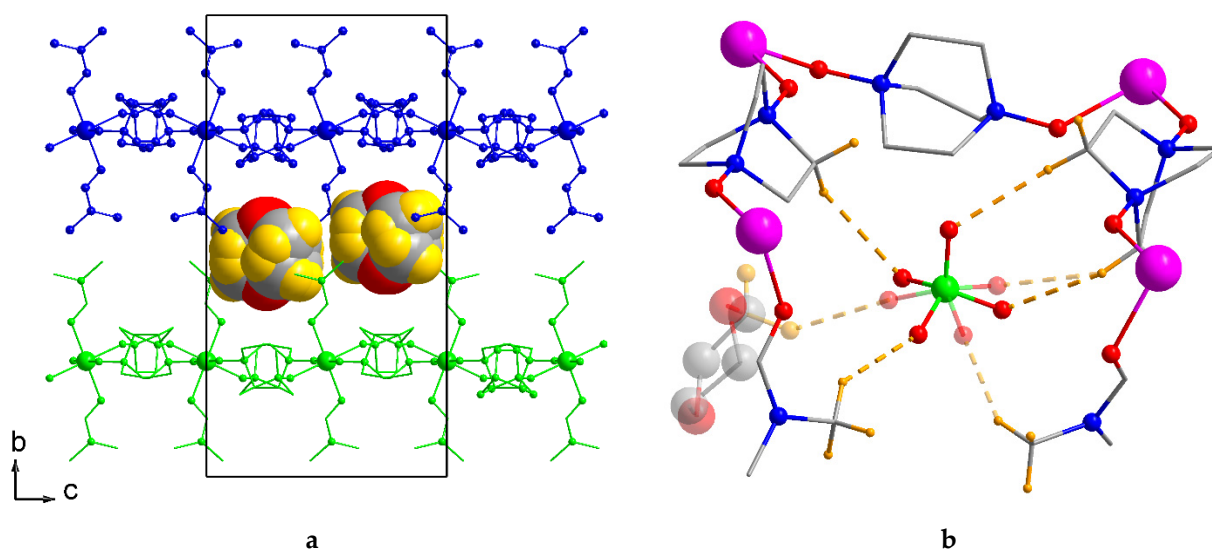


Figure 2. Crystal packing of **1**, view along the *a* axis. Each layer is shown in different colors. Dioxane molecules are shown in a space-filling mode. The black rectangle shows a projection of *b* and *c* unit cell edges (a). Closest molecular environment of perchlorate in **1**. The Cl atom is green, H atoms are orange, and other atom designations match to Figure 2. Only the H atoms relevant to ClO_4^- binding are shown for clarity, and short H...O contacts are presented by orange dashed lines. The dioxane molecule and second O positions of the disordered perchlorate are shown as semi-transparent (b).

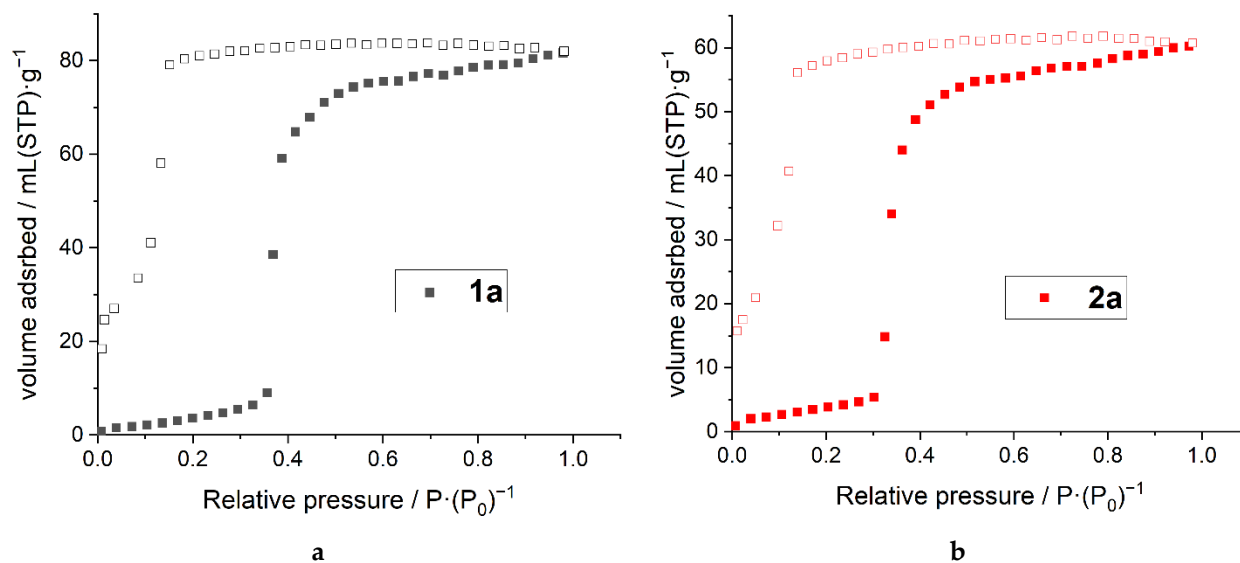


Figure 3. Carbon dioxide adsorption–desorption isotherms at 195 K for **1a** (a) and **2a** (b) (filled symbols for adsorption and open ones for desorption curves, respectively).

According to the PLATON [71] estimation, the layered coordination network in **1** and **2** possesses 20% total void volume, if erasing dioxane from the structure. The corresponding voids filled by dioxane represent holistic 1D channels, suggesting possible guest exchange and even permanent porosity of the discussed MOFs after deleting the uncharged guest molecules. Indeed, we managed to obtain porous MOF activated samples after dioxane exchange to a more volatile THF and a subsequent evacuation of the solvent. The corresponding activated samples are denoted as **1a** and **2a**. ^1H NMR spectra were recorded for the activated samples after their digestion to analyze the solvent content (Figure A3, see Appendix A). As shown in Table A1, the summary DMF and THF amounts in **1a** and **2a** are 1.61 and 1.49, respectively, lower than a number of coordinated DMF molecules in the initial **1** and **2** crystal structures (2.00). Apparently, a partial substitution of a coordinated

DMF by THF occurs upon solvent exchange. Subsequent evacuation leads to a partial evaporation of coordinated THF along with the full release of guest molecules, giving an understated amount of coordinated solvent molecules in **1a** and **2a**. However, a further resolution experiment controlled by PXRD (Figure A4 in the Appendix A) shows a full restoration of the initial PXRD pattern, illustrating a fully reversible breathing transition between the solvent-saturated crystal structure and its activated form.

2.3. Adsorption Measurements

Adsorption–desorption isotherms of carbon dioxide measured at 195 K for **1a** and **2a** are shown in Figure 3. Both investigated compounds exhibit stepped carbon dioxide isotherms, typical of the gate-opening effect or breathing behavior, with pronounced adsorption steps in 0.35–0.42, and 0.30–0.38 relative pressure ranges for **1a** and **2a**, respectively. The significant adsorption–desorption hysteresis supports this suggestion. The presence of such a type of hysteresis is typically explained by pronounced breathing in the adsorbents upon saturation, and accompanies gate-opening transitions [72–74]. The saturation volumes are ca. $81 \text{ cm}^3(\text{STP})\cdot\text{g}^{-1}$ for **1a** and $60 \text{ cm}^3(\text{STP})\cdot\text{g}^{-1}$ for **2a**. Both adsorption branches consist of two segments. The first segment corresponds to adsorption on the non-porous phase and can be described by the Brunauer–Emmett–Teller (BET) model (Figures A5 and A6; see Appendix B). The second one corresponds to adsorption on the open phase, and can be satisfactorily described by the Langmuir equation (Figures A7 and A8; see Appendix B). The monolayer capacities of non-porous forms calculated from the BET equation are 0.285 and $0.193 \text{ mmol}\cdot\text{g}^{-1}$ for **1a** and **2a**. According to Langmuir calculations after transformation into a more porous state, the monolayer capacities increase up to 4.04 and $2.98 \text{ mmol}\cdot\text{g}^{-1}$, respectively. The corresponding specific surface areas and pore volumes increase by 1–1.5 orders of magnitude (see Table 1). Nevertheless, the pore volumes, even in open form, are lower than expected volumes according to crystal structures, which were estimated to be $0.15 \text{ cm}^3\cdot\text{g}^{-1}$. This mismatch can be explained by the quite low interaction energy between the carbon dioxide and frameworks' surface. Indeed, the prediction of the interaction energy of the first adsorbate layer from the BET equation results in heats of carbon dioxide adsorption as low [75–77] as $18.5 \text{ kJ}\cdot\text{mol}^{-1}$ for **1a** and $20.2 \text{ kJ}\cdot\text{mol}^{-1}$ for **2a**. Taking into account the heat of carbon dioxide liquefaction of $16.5 \text{ kJ}\cdot\text{mol}^{-1}$, the additional energy gain is too small to provide any benefit for the full frameworks' opening. A more significant step or additional gate-opening steps are expected for other adsorbates with higher surface–adsorbate interaction energy. Moreover, gate-opening steps should be at different pressures and uptakes for different adsorbates, which allows us to consider compounds **1a** and **2a** potentially interesting systems for selective adsorption or sensing. More detailed experiments are needed, and may be presented in our further publications. The described significant breathing effects of **1a** and **2a** might be attributed to both the conformation mobility of the linker and the relative displacement motions of the layers.

Table 1. Parameters of porous structures of **1a** and **2a**.

Sample	Specific Surface Area/ $\text{m}^2\cdot\text{g}^{-1}$	$V_{\text{pore}}/\text{cm}^3\cdot\text{g}^{-1}$	$V_{\text{ads}}(\text{CO}_2)/\text{cm}^3(\text{STP})\cdot\text{g}^{-1}$
1a	$36.0^b/511^c$	$0.007^b/0.103^a$	81.8
2a	$24.4^b/377^c$	$0.006^b/0.076^a$	60.3

^a measured at $P/P_0 = 0.95$; ^b calculated for points before the adsorption step, for the closed phase; ^c calculated for points after the adsorption step, for the opened phase.

2.4. Spectroscopic Characterization

All the four samples were characterized using infrared spectroscopy. The recorded spectra (Figure 4a) contain characteristic absorption bands of the $\text{C}(\text{sp}^2)\text{--H}$ bond ($\approx 3034 \text{ cm}^{-1}$; medium); $\text{C}(\text{sp}^3)\text{--H}$ bond ($\approx 2993 \text{ cm}^{-1}$; weak) and amide C=O bond ($\approx 1662 \text{ cm}^{-1}$; strong) vibrations, all corresponding to DMF, $\text{C}(\text{sp}^3)\text{--H}$ bond vibrations ($\approx 2935 \text{ cm}^{-1}$; weak) in the

odabco aliphatic core and Cl–O bond vibrations ($\approx 1097\text{ cm}^{-1}$; very strong and $\approx 624\text{ cm}^{-1}$; strong) in the perchlorate anion [78,79]. Several absorption bands, situated in the $3420\text{--}3560\text{ cm}^{-1}$ region, are apparently attributed to O–H bond vibrations, originating from some possible watering of the samples during their storage and preparation for IR measurements. Therefore, the infrared spectra of all the four compounds are entirely similar to each other and confirm their molecular composition. In particular, the presented IR data show no considerable changes in the chemical nature of the activated samples **1a** and **2a**, compared to their solvent-filled parents **1** and **2**.

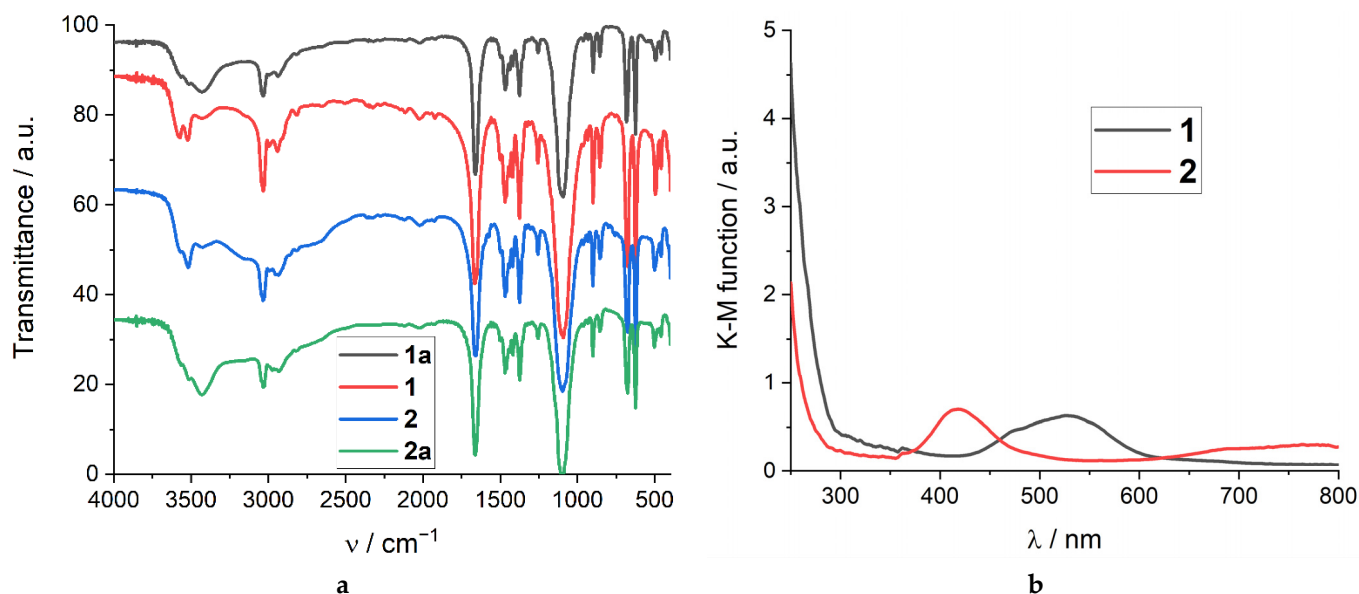


Figure 4. Infrared spectra of dry samples **1**, **2**, **1a** and **2a** (a). Diffuse reflectance spectra of the dry **1** and **2**, recalculated to K–M(λ) dependencies (b).

The UV/vis absorption of solid **1** and **2** was investigated via diffuse reflectance spectroscopy (DRS). As shown in Figure 4b, compound **1** possesses one absorption band in the green region with $\lambda_{\text{max}} = 530\text{ nm}$, apparently corresponding to $d\text{--}d$ electron transitions in Co^{2+} , hexa-coordinated by oxygen [80,81] and providing its pink color as a mixture of low-wavelength violet and high-wavelength red color components. Oppositely, the DRS spectrum of **2** contains an absorption band in the violet-blue region with $\lambda_{\text{max}} = 418\text{ nm}$ and a very wide weak band in the red/NIR area ($\lambda_{\text{max}} \approx 776\text{ nm}$), providing a green color quite typical of Ni^{2+} complexes with an octahedral [82,83] oxygen environment. No bands attributed to other molecular constituents were found for both **1** and **2**, as the odabco aliphatic ligand possesses negligible absorption, even in the UVB region, due to the absence of any conjugated π -system. Moreover, the expectedly weak extinction of both DMF and perchlorate is apparently overlapped by the optical absorption of the air medium, arising in the hard UVC area.

2.5. Magnetization Measurements

The temperature dependences of the magnetic susceptibility $\chi_p(T)$ were measured to examine the spin states of metal centers and to analyse the possible magnetic interactions between them. As can be seen in Figure 5, compounds **1** and **1a** demonstrate a paramagnetic behavior in the entire temperature range $1.77\text{--}300\text{ K}$, without any anomaly that could be attributed to the magnetic ordering of Co^{2+} ions. However, the $\chi_p(T)$ pattern deviates from the simple Curie–Weiss law, which implies that the magnetic moments of Co^{2+} ions are temperature-dependent. Indeed, the effective magnetic moment μ_{eff} formally calculated for **1** gradually decreases from $\mu_{\text{eff}} = 4.78\ \mu_B$ at $T = 300\text{ K}$ down to $\mu_{\text{eff}} = 3.81\ \mu_B$ at $T = 1.77\text{ K}$ (Figure 5a). The high-temperature $\mu_{\text{eff}} = 4.78\ \mu_B$ agrees well with the values commonly observed for octahedrally coordinated Co^{2+} ions with a high-spin configuration

($S = 3/2$) and a considerable contribution of orbital moments [84]. The strong decrease in the effective magnetic moment observed on cooling originates predominantly from the zero-field-splitting (ZFS) of Co^{2+} ion levels [85]. It is worth emphasizing that in the lowest temperature region, the $\mu_{\text{eff}}(T)$ dependence slows down, and μ_{eff} saturates at a temperature-independent level (inset in Figure 5a). This is direct evidence of a negligible interaction between Co^{2+} ions. In fact, as soon as the single-ion parameters are finally settled at low temperatures, the $\chi_p(T)$ dependence acquires a simple Curie shape $\chi_p = C/T$, i.e., the behavior of an ideal paramagnet with a negligible interaction between ions. Therefore, the paramagnetic behavior of **1** is entirely consistent with its crystal structure, which comprises the only spatially separated metal ions with the intermetal distances exceeding 8.2 Å. Such distances are too high to provide any considerable exchange occurring between single Co^{2+} ions. The activated sample **1a** demonstrates almost the same behavior (Figure 5b), with the corresponding values of $\mu_{\text{eff}} = 4.69 \mu_B$ at $T = 300 \text{ K}$ and $\mu_{\text{eff}} = 3.75 \mu_B$ at $T = 1.77 \text{ K}$.

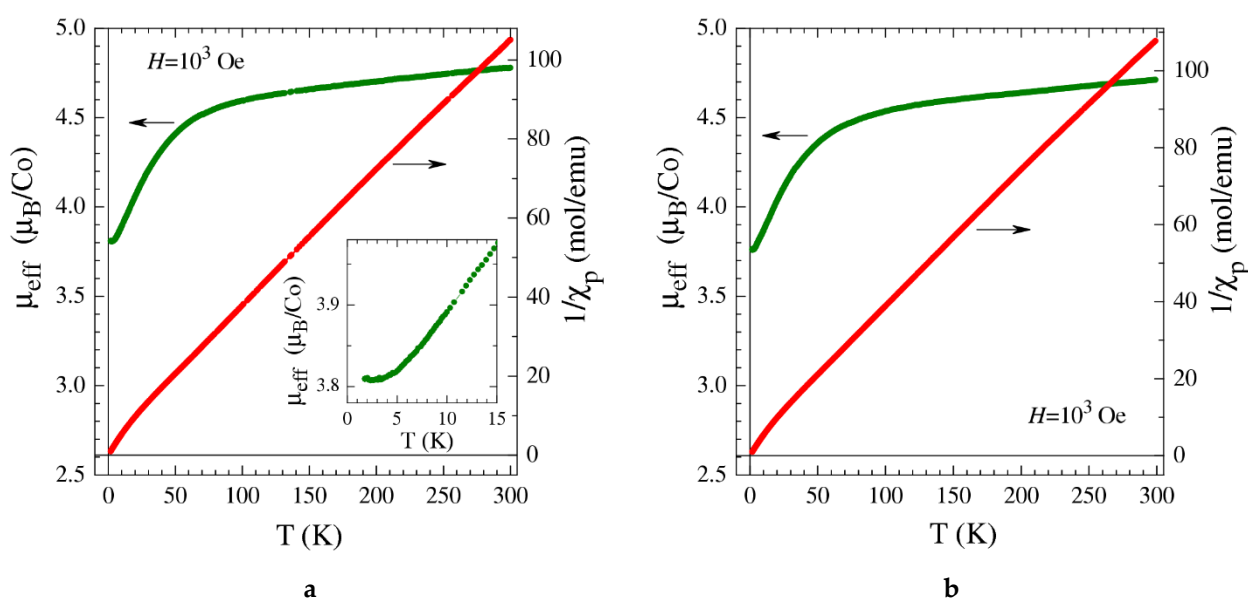


Figure 5. Temperature dependencies of the inversed magnetic susceptibility $1/\chi_p(T)$ and effective magnetic moment $\mu_{\text{eff}}(T)$ for **1** (a) and **1a** (b). The inset in (a) shows the low- T $\mu_{\text{eff}}(T)$ data on an enlarged scale.

The $\chi_p^{-1}(T)$ and $\mu_{\text{eff}}(T)$ dependences measured for the samples **2** and **2a** also confirm their paramagnetic behavior (Figure 6). The effective magnetic moment for **2** is $\mu_{\text{eff}} = 3.32 \mu_B$ at $T = 300 \text{ K}$, and slightly exceeds the theoretical spin-only value of $\mu_{\text{eff}} = 2.83 \mu_B$ for Ni^{2+} ($S = 1$) ions in the octahedral coordination environment. Such a difference is not surprising and can be explained by the spin–orbital coupling, which, however, for Ni^{2+} is typically weaker than for Co^{2+} . The μ_{eff} value for **2** gradually lowers upon cooling and reaches a $3.22 \mu_B$ value at $T = 30 \text{ K}$, presumably following the decreasing contribution of the orbital moment. Upon further lowering the temperature, the effective magnetic moment of **2** sharply drops down to $2.15 \mu_B$ at $T = 1.77 \text{ K}$. Such a steep μ_{eff} decrease may come from the zero-field level-splitting (expected for Ni^{2+} ($S = 1$) ions), as well as from a weak antiferromagnetic exchange interaction between metal ions. Analysis of the $\mu_{\text{eff}}(T)$ dependence has shown that it cannot be fitted if only the exchange interaction is taken into account, yet a good fit (dashed lines in Figure 6) can be obtained if zero-field splitting with the axial ZFS parameter $D/k_B \approx 7.4 \text{ K}$ is introduced, following the approach described in Ref. [85], together with a small additional intermetal exchange interaction $zJ/k_B \approx 0.17 \text{ K}$ (z is the number of nearest neighbors). The obtained D value is typical of Ni(II) complexes [86], while the small zJ value may indicate a tiny intermetal magnetic exchange in **2**. Given the immeasurably low exchange interaction found in isostructural Co compounds, it is not

certain whether the small additional term observed for **2** is actually reflecting the intermetal exchange, or if it comes from an unaccounted single-ion feature. Whatever the case, we can conclude that the magnetic behavior of **2** is close to that of an ideal paramagnet, with the J/k_B certainly less than 0.1 K. The magnetic behavior of the activated sample **2a** is similar to its parent **2** (with just slightly lower D/k_B of 6.3 K; see Figure 6b), ensuring full preservation of the layered coordination network during the evacuation of the guest solvent.

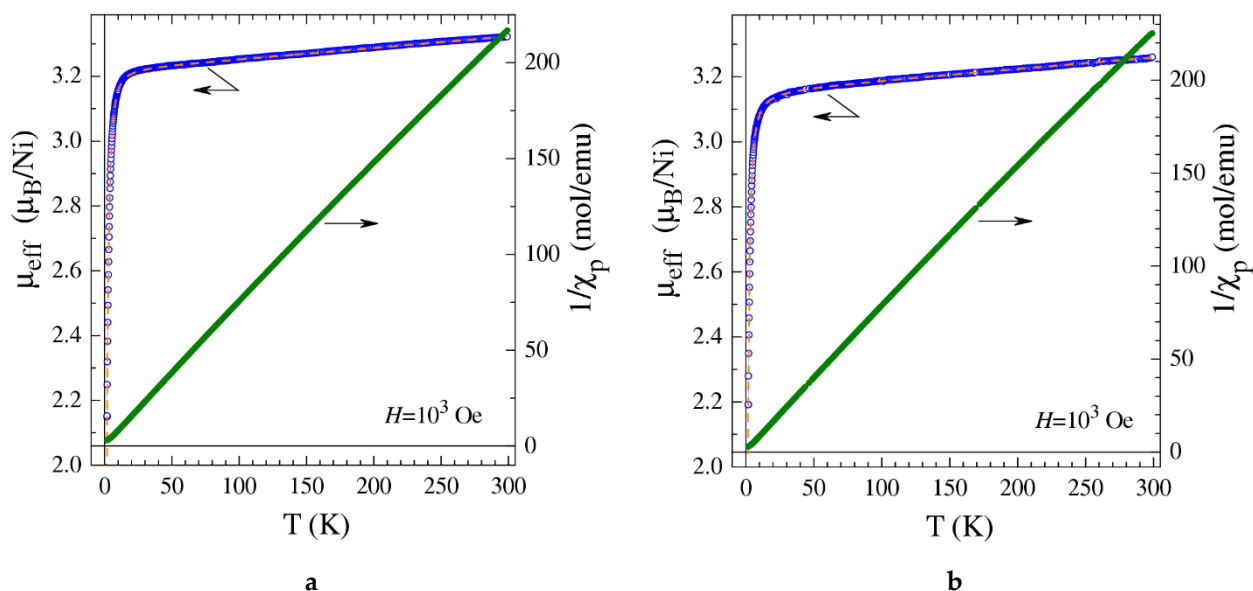


Figure 6. Temperature dependencies of the inversed magnetic susceptibility $\chi_p^{-1}(T)$ and effective magnetic moment $\mu_{\text{eff}}(T)$ for **2** (a) and **2a** (b). The dashed lines shows the numerical fits to the $\mu_{\text{eff}}(T)$ data as described in the text.

3. Materials and Methods

3.1. Materials

Cobalt(II) perchlorate hexahydrate, nickel(II) perchlorate hexahydrate, *N,N*-dimethylformamide (DMF) and dioxane, all of reagent grade, were supplied by Vekton (Saint Petersburg, Russia). Perchloric acid (HClO_4 ; 65% water solution, reagent grade) was supplied by Rechem (Moscow, Russia). Tetrahydrofuran (THF; reagent grade, hydroquinone-stabilized) was supplied by Reaktiv (Novosibirsk, Russia). Odabco $\cdot 3\text{H}_2\text{O}_2$ was synthesized according to the previously published procedure [45].

3.2. Instruments

Infrared (IR) spectra were obtained in the range of 4000–400 cm^{-1} on a Bruker Scimitar FTS 2000 spectrometer in KBr pellets. Elemental CHNS analyses were carried out using a VarioMICROcube device. Powder X-ray diffraction (PXRD) data were acquired on a Shimadzu XRD-7000 diffractometer ($\text{Cu-K}\alpha$ radiation, $\lambda = 1.54178 \text{ \AA}$) at room temperature. Diffuse reflectance spectra were recorded using a Shimadzu UV-3101 spectrometer. The initial dependencies of the reflection of samples (R) on the wavelength were recalculated with the Kubelka–Munk function (M) using the equation: $M = (1 - R)^2/2R$. A small shift in the curves of the DR spectra at $\lambda = 360 \text{ nm}$ is an instrumental error and related to the switching of the light source in the spectrometer. ^1H NMR spectra were recorded on a Bruker Advance 500 NMR spectrometer (500.13 Hz). The analyte solutions for NMR were prepared by dissolving ca. 5 mg of **1a** and **2a** in 0.8 mL of D_2O , then adding a ca. 15 times excess of NaOH dissolved in 0.4 mL of D_2O , followed by a careful decantation of the liquids from metal hydroxide precipitates.

The porous structure was analyzed using carbon dioxide adsorption on a Quantachrome's Autosorb iQ gas sorption analyzer at 195 K. A CryoCoolerTM cryostat was used

to control the sample temperature at 195 K, with 0.05 K accuracy. Initially, the compound was activated under a dynamic vacuum at 50 °C for 6 h. Weight loss during the activation procedure was 9.9% and 7.5% for compounds **1a** and **2a** correspondingly, which is in a good agreement with loss of guest THF molecules. The carbon dioxide adsorption–desorption isotherms were measured within the range of relative pressures from 10^{-3} to 0.995. The specific surface area was calculated from the data obtained using conventional Langmuir and BET models. Pore volumes were calculated as the amount of vapor adsorbed at a relative pressure close to unity for open form and $P/P_0 = 0.3$ for closed form, assuming that the pores are filled with a liquid adsorbate.

Diffraction data for single crystals of **1** and **2** were collected on an automated Agilent Xcalibur diffractometer equipped with an AtlasS2 area detector and graphite monochromator ($\lambda(\text{MoK}\alpha) = 0.71073 \text{ \AA}$). The CrysAlisPro program package [87] was used for the integration, absorption correction, and determination of unit cell parameters. A dual-space algorithm (SHELXT [88]) was used for structure solution, and a full-matrix least squares technique (SHELXL [89]) was used for structure refinement. Anisotropic approximation was applied for all atoms except hydrogens. The positions of hydrogen atoms of organic ligands were calculated geometrically and refined in the riding model. Details for single crystal structure determination experiments and structure refinements are summarized in Table A2 (See Appendix C). CCDC 2,264,393 (**1**) and 2,264,394 (**2**) entries contain the supplementary crystallographic data for this paper. These data can be obtained free of charge from The Cambridge Crystallographic Data Center at <https://www.ccdc.cam.ac.uk/structures/> (accessed on 16 May 2023).

Magnetization measurements were performed using a Quantum Design MPMS-XL SQUID magnetometer in the temperature range of 1.77–300 K at magnetic fields up to 10 kOe. In order to determine the paramagnetic component of the molar magnetic susceptibility, $\chi_p(T)$, the temperature-independent diamagnetic contribution, χ_d , and a possible magnetization of ferromagnetic micro-impurities, $\chi_{\text{FM}}(T)$, were evaluated and subtracted from the measured values of the total molar susceptibility, $\chi = M/H$. While χ_d was calculated using the Pascal's additive scheme, $\chi_{\text{FM}}(T)$, if any, was determined from the measured isothermal $M(H)$ dependencies and the $M(T)$ data taken in different magnetic fields. To determine the effective magnetic moment (μ_{eff}), temperature dependences $\chi_p(T)$ were analyzed using the Curie–Weiss dependence:

$$\chi_p(T) = N_A \mu_{\text{eff}}^2 / 3k_B(T - \theta)$$

where N_A and k_B are the Avogadro number and the Boltzmann constant, respectively.

3.3. Synthetic Methods

Care should be taken in all the procedures carried out with 1,4-diazabicyclo[2.2.2]octane N,N' -dioxide tris-(hydrogen peroxide) solvate (odabco·3H₂O₂) and odabco compounds with potentially explosive anions such as perchlorate.

Synthesis of [Co(DMF)₂(odabco)₂](ClO₄)₂·dioxane (**1**). 70 mg (0.20 mmol) of Co(ClO₄)₂·6H₂O, 49 mg (0.20 mmol) of odabco·3H₂O₂, and 2.5 mL of DMF, 2.5 mL of dioxane and 40 μL of HClO₄ (65% solution in water) were mixed in a glass vial with a screw cap. The mixture was treated in an ultrasonic bath upon full dissolution (*ca.* for 5 min) and then heated at 90 °C for 48 h. The formed pink crystals were filtered on a porous paper filter, washed with DMF, then with dioxane, and dried in air. Single crystals suitable for the SCXRD were taken from the mother liquor before the filtration. Yield: 64 mg (42%). Elemental analysis data (%): C, 29.8; H, 5.6; N, 10.7; Cl, 9.2. Calculated for [Co(DMF)₂(odabco)₂](ClO₄)₂·0.3dioxane·3H₂O (%): C, 29.8; H, 6.1; N, 10.9; Cl, 9.2.

Synthesis of [Ni(DMF)₂(odabco)₂](ClO₄)₂·dioxane (**2**) was carried out analogously to the synthesis of **1**, except changing Co(ClO₄)₂·6H₂O to a similar amount as Ni(ClO₄)₂·6H₂O. The formed light green crystals were filtered on the porous paper filter, washed with DMF, then with dioxane, and dried in air. Single crystals suitable for the SCXRD were taken from the mother liquor before the filtration. Yield: 57 mg (37%). Elemental analysis data (%): C,

33.6; H, 5.9; N, 10.8; Cl, 9.5. Calculated for $[\text{Ni}(\text{DMF})_2(\text{odabco})_2](\text{ClO}_4)_2 \cdot \text{dioxane}$ (%): C, 33.9; H, 5.9; N, 10.8; Cl, 9.1.

Synthesis of activated **1a**. A ca. 60 mg sample of **1** was immersed in 5.0 mL of THF. The solvent was refreshed once after two days of immersion. After four days, the sample was filtered, washed with THF, and dried in air.

Synthesis of activated **2a** was carried out using a similar procedure carried out with **2** instead of **1**.

4. Conclusions

To summarize, two new metal–organic frameworks based on a highly flexible 1,4-diazabicyclo[2.2.2]octane N,N' -dioxide bridging ligand were synthesized and characterized using a combination of X-ray diffraction, chemical analysis, spectroscopic analysis, gas adsorption, and magnetization methods. Compounds possess layered cationic coordination networks and preserve their gas adsorption capability in the activated state, driven by gate-opening transitions upon CO_2 saturation. Magnetization measurement results, along with other experimental data, confirm coordination network structure preservation within the activated samples and reveal a cation-dependent magnetization behavior. Zero-field level-splitting, which prompts a decrease in the effective magnetic moments of metal ions at low temperatures, was found for both the nickel(II)- and cobalt-based compounds.

Author Contributions: Conceptualization, P.A.D.; methodology, P.A.D., A.N.L., K.A.K. and V.P.F.; software, K.A.K.; validation, P.A.D., A.N.L., K.A.K. and V.P.F.; formal analysis, P.A.D., A.N.L. and K.A.K.; investigation, P.A.D., A.N.L. and K.A.K.; resources, V.P.F.; data curation, P.A.D. and V.P.F.; writing—original draft preparation, P.A.D., A.N.L. and K.A.K.; writing—review and editing, V.P.F.; visualization, P.A.D., A.N.L. and K.A.K.; project administration, V.P.F.; funding acquisition, V.P.F. All authors have read and agreed to the published version of the manuscript.

Funding: The authors are grateful to the Ministry of Science and Higher Education of the Russian Federation for financial support (Agreement No. 075-15-2022-263), and for providing access to the large-scale research facility “EXAFS spectroscopy beamline”.

Data Availability Statement: CCDC 2264393 (**1**) and 2264394 (**2**) contain the supplementary crystallographic data for this paper. These data can be obtained free of charge at Cambridge Crystallographic Data Center (<https://www.ccdc.cam.ac.uk/structures/>; accessed on 16 May 2023), or from the authors upon request.

Conflicts of Interest: The authors declare no conflict of interest.

Appendix A. Additional Characterization Data

Table A1. Assignment for ^1H NMR spectra for **1a** and **2a**.

Peak Position, ppm	Integral, a.u.	Assignment	Amount in One Molecule	Molecular Units, a.u. *
8.37 (1a) 8.39 (2a)	1.000	H_{CO} (DMF)	1	1.44 DMF (1a) 1.43 DMF (2a)
2.19 (1a) 2.22 (2a)	6.519 (1a) 6.635 (2a)	H_{CH_3} (DMF)	6	
3.89 (1a) 3.89 (2a)	18.133 (1a) 18.075 (2a)	H_{CH_2} (odabco)	12	2.00 odabco (1a and 2a)
3.67 (1a) 3.69 (2a)	0.488 (1a) 0.179 (2a)	$\text{H}_{\text{CH}_2\text{O}}$ (THF)	4	0.17 THF (1a) 0.06 THF (2a)
1.80 (1a) 1.82 (2a)	0.516 (1a) 0.176 (2a)	$\text{H}_{\text{CH}_2\text{CH}_2}$ (THF)	4	

* Molecular constituent contents were normalized for the odabco amount to 2.00 for clarity.

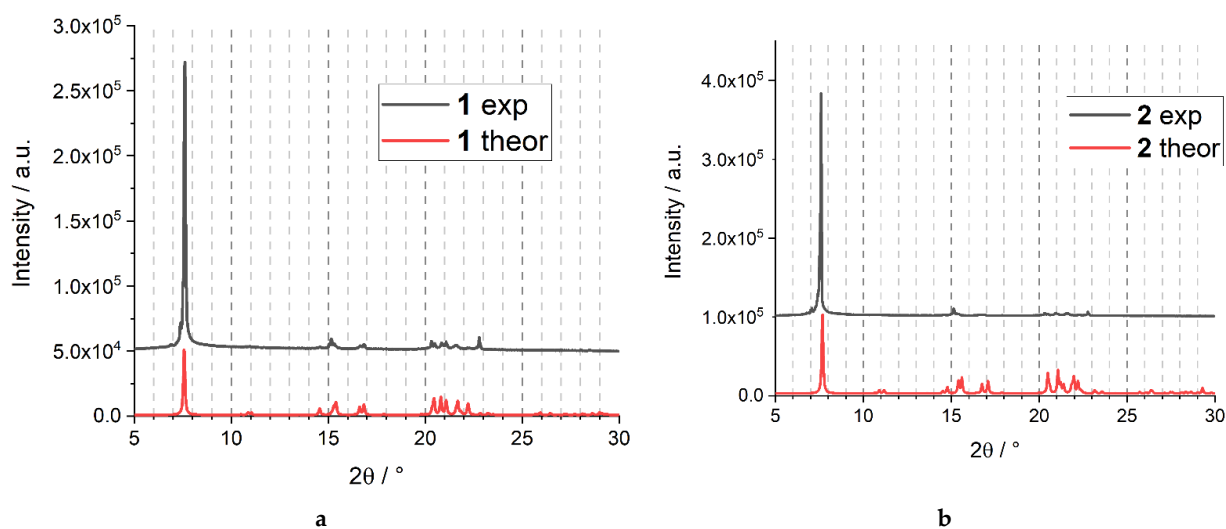


Figure A1. Experimental PXRD patterns of the filtered samples 1 (a) and 2 (b) compared to the theoretical samples.

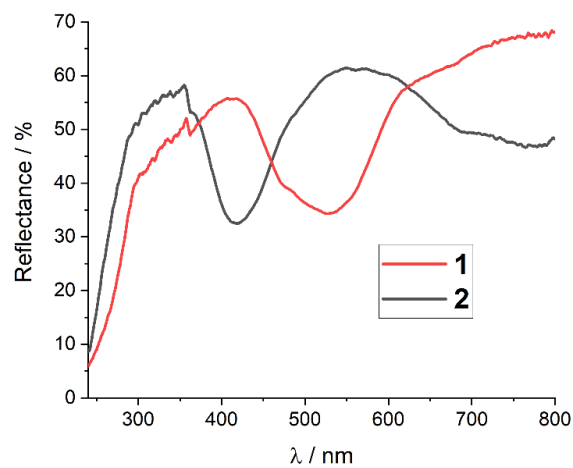


Figure A2. Diffuse reflectance spectra of the dry 1 and 2 in $R(\lambda)$ dependencies.

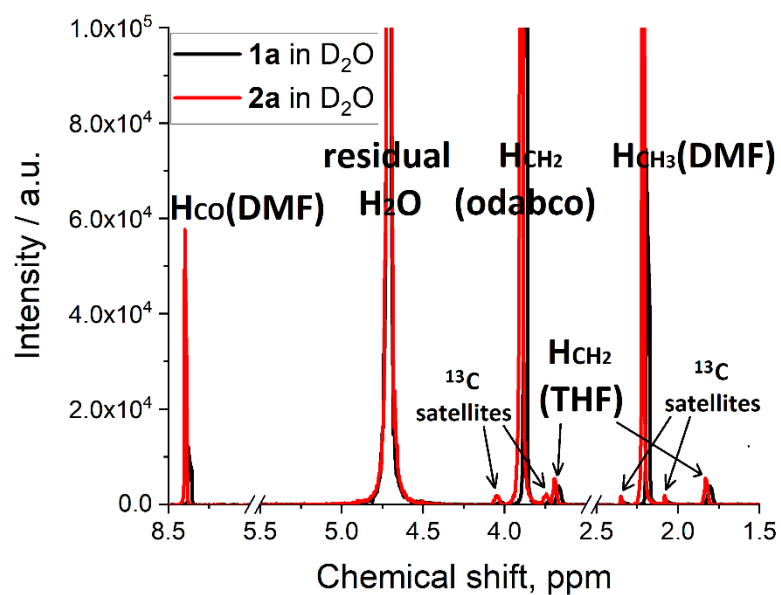


Figure A3. ^1H NMR spectra of 1a and 2a digested in $\text{D}_2\text{O}/\text{KOH}$.

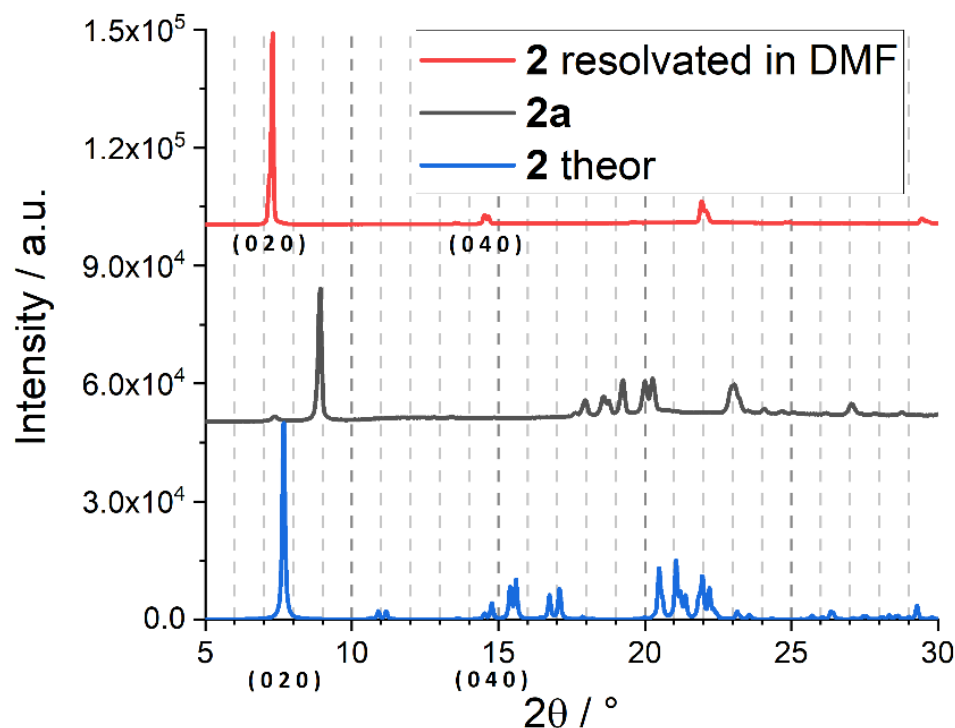


Figure A4. PXRD patterns of activated **2a** and resolvated **2** compared to the theoretical PXRD pattern.

Appendix B. Adsorption Supplementary Data

Appendix B.1. BET Calculations

According to BET theory, the adsorption isotherm may be described by this equation:

$$\frac{1}{n \cdot \left(\frac{P_0}{P} - 1 \right)} = \frac{1}{w \cdot C} + \frac{C - 1}{w \cdot C} \cdot \frac{P}{P_0}$$

where n —amount adsorbed [mmol/g], w —monolayer capacity [mmol/g], C —BET constant, P/P_0 —relative pressure.

The specific surface area of the sample can be expressed as

$$S_{\text{BET}} = w \cdot N_A \cdot A_{cs}$$

where N_A —Avogadro's number, A_{cs} —cross-sectional area (21.0 Å² for CO₂).

The interaction energy of the first adsorbate layer can be calculated from the BET constant C , which is an energetic characteristic of adsorption:

$$C = \exp \left[\frac{E_1 - E_L}{RT} \right]$$

where E_1 —the interaction energy of the first adsorbate layer, E_L —the heat of liquefaction.

According to these equations, the specific surface area and the interaction energy of the first adsorbate layer were evaluated for the closed forms of the compounds **1a** and **2a**.

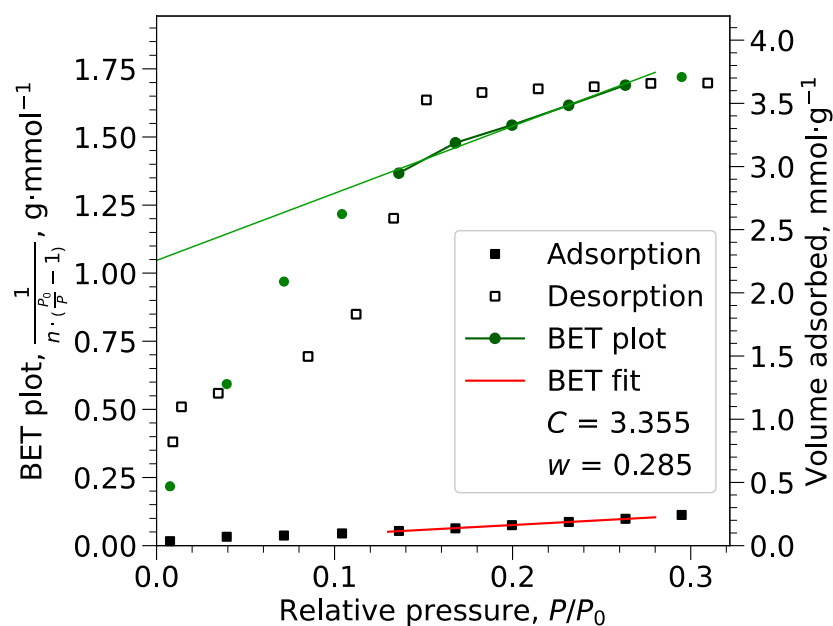


Figure A5. BET calculation plots for **1a** (C —BET constant, w —monolayer capacity in $\text{mmol}\cdot\text{g}^{-1}$).

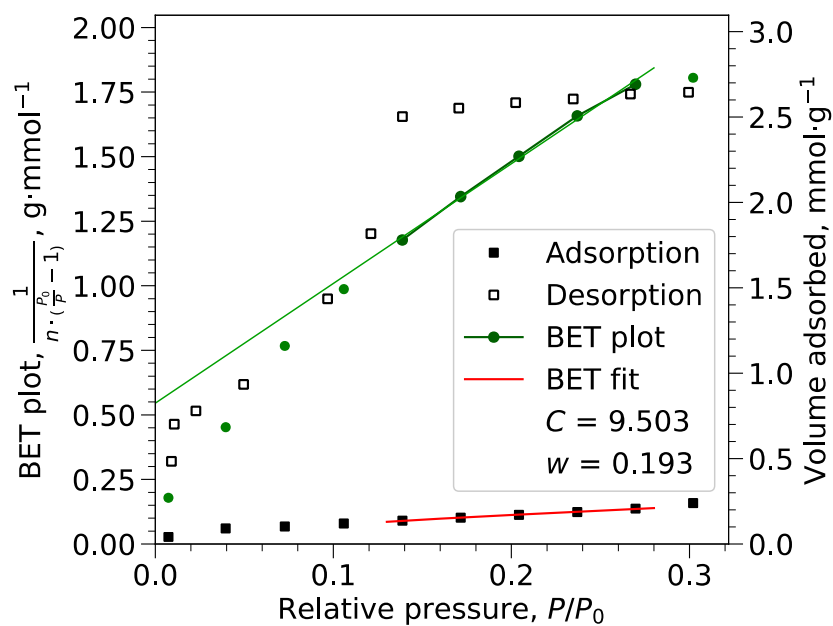


Figure A6. BET calculation plots for **2a** (C —BET constant, w —monolayer capacity in $\text{mmol}\cdot\text{g}^{-1}$).

Appendix B.2. Langmuir Calculations

The Langmuir equation can be expressed as

$$\frac{P/P_0}{n} = \frac{1}{w \cdot K} + \frac{P/P_0}{w}$$

where n —amount adsorbed [mL/g], w —monolayer capacity [mL/g], K —Langmuir equilibrium constant, P/P_0 —relative pressure.

The specific surface area can be calculated from the monolayer capacity using the same equation as in the BET method.

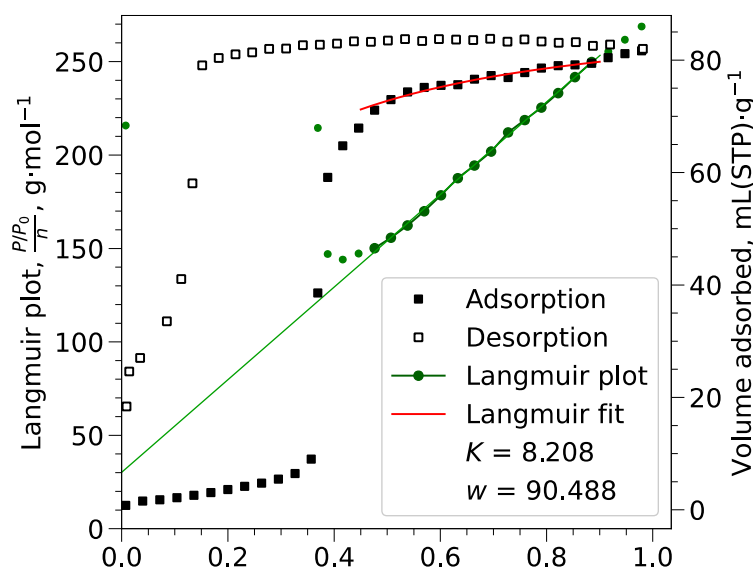


Figure A7. Langmuir calculation plots for 1a (K —Langmuir equilibrium constant, w —monolayer capacity in mL (STP)·g⁻¹).

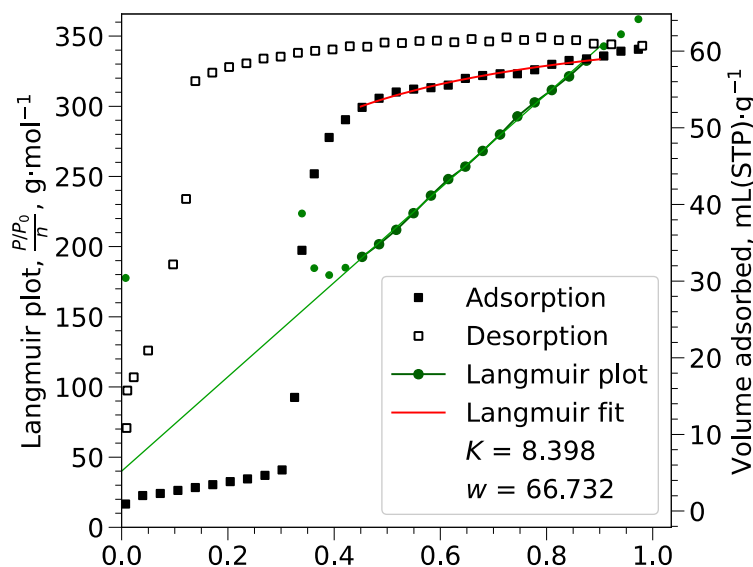


Figure A8. Langmuir calculation plots for 2a (K —Langmuir equilibrium constant, w —monolayer capacity in mL (STP)·g⁻¹).

Appendix B.3. Pore Volumes

The volume of carbon dioxide adsorbed (V_{ads}) can be converted to the volume of condensed carbon dioxide, which is assumed to be equal to the pore volume:

$$V_{\text{pore}} = \frac{V_{\text{ads}}}{V_M} \cdot \frac{M}{\rho} = \frac{V_{\text{ads}}}{V_M} \cdot V_m$$

where V_M —the molar volume of gas at STP (22.414 cm³/mol), M —the adsorbate molar mass (44.01 g/mol), ρ —the density of condensed carbon dioxide (1.564 g·cm⁻³), V_m —the molar volume of the condensed carbon dioxide (28.14 cm³/mol).

Appendix C. The Crystallographic Data

Table A2. Single crystal X-ray determination and structure refinement details.

	1	2
Chemical formula	C ₂₂ H ₄₆ Cl ₂ CoN ₆ O ₁₆	C ₂₂ H ₄₆ Cl ₂ N ₆ NiO ₁₆
$M_r/\text{g}\cdot\text{mol}^{-1}$	780.48	780.26
Crystal system	Monoclinic	Monoclinic
Space group	C2/c	C2/c
Temperature/K	237	130
$a/\text{Å}$	12.1805(6)	12.1891(3)
$b/\text{Å}$	23.3427(14)	23.0318(6)
$c/\text{Å}$	12.1557(5)	11.9842(3)
$\alpha/^\circ$	90	90
$\beta/^\circ$	90.975 (4)	91.577 (2)
$\gamma/^\circ$	90	90
$V/\text{Å}^3$	3455.7(3)	3363.13(15)
Z	4	4
F(000)	1636	1640
$D(\text{calc.})/\text{g}\cdot\text{cm}^{-3}$	1.500	1.541
μ/mm^{-1}	0.73	0.81
Crystal size/mm	0.40 × 0.40 × 0.06	0.27 × 0.25 × 0.07
θ range for data collection/ $^\circ$	1.87 ≤ θ ≤ 25.35	3.34 ≤ θ ≤ 25.34
No. of reflections: measured/independent/observed [$I > 2\sigma(I)$]	7638/3175/2606	7249/3081/2696
R_{int}	0.0255	0.0170
Index ranges	−14 ≤ h ≤ 14 −28 ≤ k ≤ 23 −14 ≤ l ≤ 12	−14 ≤ h ≤ 14 −27 ≤ k ≤ 19 −13 ≤ l ≤ 14
Final R indices [$I > 2\sigma(I)$]	$R_1 = 0.0474$ $wR_2 = 0.1125$	$R_1 = 0.0295$ $wR_2 = 0.0757$
Final R indices (all data)	$R_1 = 0.0627$ $wR_2 = 0.1211$	$R_1 = 0.0362$ $wR_2 = 0.0788$
Goodness-of-fit on F^2	1.034	1.058
Largest diff. peak, hole/ $e\cdot\text{Å}^{-3}$	0.48, −0.42	0.34, −0.44

References

- Ghasempour, H.; Wang, K.-Y.; Powell, J.A.; ZareKarizi, F.; Lv, X.-L.; Morsali, A.; Zhou, H.-C. Metal–organic frameworks based on multicarboxylate linkers. *Coord. Chem. Rev.* **2021**, *426*, 213542. [[CrossRef](#)]
- Yang, D.; Chen, Y.; Su, Z.; Zhang, X.; Zhang, W.; Srinivas, K. Organic carboxylate-based MOFs and derivatives for electrocatalytic water oxidation. *Coord. Chem. Rev.* **2021**, *428*, 213619. [[CrossRef](#)]
- Desai, A.V.; Sharma, S.; Let, S.; Ghosh, S.K. N-donor linker based metal-organic frameworks (MOFs): Advancement and prospects as functional materials. *Coord. Chem. Rev.* **2019**, *395*, 146–192. [[CrossRef](#)]
- Raptopoulou, C.P. Metal-Organic Frameworks: Synthetic Methods and Potential Applications. *Materials* **2021**, *14*, 310. [[CrossRef](#)]
- Sharma, S.; Dutta, S.; Dam, G.K.; Ghosh, S.K. Neutral Nitrogen Donor Ligand-based MOFs for Sensing Applications. *Chem. Asian J.* **2021**, *16*, 2569–2587. [[CrossRef](#)]
- Kamal, S.; Khalid, M.; Shah Nawaz Khan, M.; Shahid, M.; Ahmad, M. A bifunctionalised Pb-based MOF for iodine capture and dye removal. *Dalton Trans.* **2023**, *52*, 4501–4516. [[CrossRef](#)]

7. Lysova, A.A.; Kovalenko, K.A.; Nizovtsev, A.S.; Dybtsev, D.N.; Fedin, V.P. Efficient separation of methane, ethane and propane on mesoporous metal-organic frameworks. *Chem. Eng. J.* **2023**, *453*, 139642. [[CrossRef](#)]
8. Li, X.L.; Fang, D.; Lieu, W.Y.; Chen, C.; Shah Nawaz Khan, M.; Li, D.-S.; Tian, B.; Shi, Y.; Yang, H.Y. Metal-Organic-Framework-Derived 3D Hierarchical Matrixes for High-Performance Flexible Li-S Batteries. *ACS Appl. Mater. Interfaces* **2023**, *15*, 20064–20074. [[CrossRef](#)]
9. Shi, Y.; Zou, Y.; Shah Nawaz Khan, M.; Zhang, M.; Yan, J.; Zheng, X.; Wang, W.; Xie, Z. Metal-organic framework-derived photoelectrochemical sensors: Structural design and biosensing technology. *J. Mater. Chem. C* **2023**, *11*, 3692–3709. [[CrossRef](#)]
10. Matyukhina, A.K.; Zorina-Tikhonova, E.N.; Goloveshkin, A.S.; Babeshkin, K.A.; Efimov, N.N.; Kiskin, M.A.; Eremenko, I.L. Field-Induced Slow Magnetic Relaxation in Co^{II} Cyclopropane-1,1-dicarboxylates. *Molecules* **2022**, *27*, 6537. [[CrossRef](#)]
11. Tepper, R.; Schulze, B.; Bellstedt, P.; Heidler, J.; Görls, H.; Jäger, M.; Schubert, U.S. Halogen-bond-based cooperative ion-pair recognition by a crown-ether-embedded 5-iodo-1,2,3-triazole. *Chem. Commun.* **2017**, *53*, 2260–2263. [[CrossRef](#)] [[PubMed](#)]
12. Czugler, M.; Pintér, I. Sodium halide complexes of ribose derivatives and their unusual crystal structures. *Carbohydr. Res.* **2011**, *346*, 1610–1616. [[CrossRef](#)] [[PubMed](#)]
13. Marabello, D.; Antoniotti, P.; Benzi, P.; Beccari, F.; Canepa, C.; Cariati, E.; Cioci, A.; Lo Presti, L. Crystal structure or chemical composition of salt-sugar-based metal-organic frameworks: What are the nonlinear optical properties due to? *Acta Crystallogr.* **2021**, *B77*, 506–514. [[CrossRef](#)]
14. Jiang, W.; Liu, H.; Liao, Q.; Tang, T.; Liu, J.; Liu, Z.; Xie, L.; Yan, J. Preparation of two metal organic frameworks (K-β-CD-MOFs and Cs-β-CD-MOFs) and the adsorption research of myricetin. *Polyhedron* **2021**, *196*, 114983. [[CrossRef](#)]
15. Koshevoy, E.I.; Samsonenko, D.G.; Berezin, A.S.; Fedin, V.P. Metal-Organic Coordination Polymers Formed from γ-Cyclodextrin and Divalent Metal Ions. *Eur. J. Inorg. Chem.* **2019**, *2019*, 4321–4327. [[CrossRef](#)]
16. Govindaraj, M.; Huang, W.-C.; Lee, C.-Y.; Lakshmanan, V.; Liu, Y.-H.; So, P.B.; Lin, C.-H.; Chen, J.-D. Structural Diversity of Mercury(II) Halide Complexes Containing Bis-pyridyl-bis-amide with Bulky and Angular Backbones: Ligand Effect and Metal Sensing. *Int. J. Mol. Sci.* **2022**, *23*, 7861. [[CrossRef](#)]
17. Wang, J.; Zhang, X.; Liang, F.; Hu, Z.; Wu, Y. Co-crystal AX·(H₃C₃N₃O₃) (A = Na, Rb, Cs; X = Br, I): A series of strongly anisotropic alkali halide cyanurates with a planar structural motif and large birefringence. *Dalton Trans.* **2021**, *50*, 11555–11561. [[CrossRef](#)]
18. Li, Z.-F.; Liang, L.-L.; Wu, F.; Zhou, F.-G.; Ni, X.-L.; Feng, X.; Xiao, X.; Zhang, Y.-Q.; Xue, S.-F.; Zhu, Q.-J.; et al. An approach to networks based on coordination of alkyl-substituted cucurbit[5]urils and potassium ions. *CrystEngComm* **2013**, *15*, 1994–2001. [[CrossRef](#)]
19. Shen, N.; Yang, Z.; Liu, S.; Dai, X.; Xiao, C.; Taylor-Pashow, K.; Li, D.; Yang, C.; Li, J.; Zhang, Y.; et al. ⁹⁹TcO₄⁻ removal from legacy defense nuclear waste by an alkaline-stable 2D cationic metal organic framework. *Nat. Commun.* **2020**, *11*, 5571. [[CrossRef](#)]
20. Ma, J.; Wang, C.-C.; Zhao, Z.-X.; Wang, P.; Li, J.-J.; Wang, F.-X. Adsorptive capture of perhenate (ReO₄⁻) from simulated wastewater by cationic 2D-MOF BUC-17. *Polyhedron* **2021**, *202*, 115218. [[CrossRef](#)]
21. Yu, C.-X.; Chen, J.; Zhang, Y.; Song, W.-B.; Li, X.-Q.; Chen, F.-J.; Zhang, Y.-J.; Liu, D.; Liu, L.-L. Highly efficient and selective removal of anionic dyes from aqueous solution by using a protonated metal-organic framework. *J. Alloys Compd.* **2021**, *853*, 157383. [[CrossRef](#)]
22. Li, X.; Zhang, S.; Zhang, L.; Yang, Y.; Zhang, K.; Cai, Y.; Xu, Y.; Gai, Y.; Xiong, K. Viologen-Based Cationic Metal-Organic Framework for Antibiotics Detection and MnO₄⁻ Removal in Water. *Cryst. Growth Des.* **2022**, *22*, 3991–3997. [[CrossRef](#)]
23. Li, J.; Yuan, S.; Qin, J.-S.; Pang, J.; Zhang, P.; Zhang, Y.; Huang, Y.; Drake, H.F.; Liu, W.R.; Zhou, H.-C. Stepwise Assembly of Turn-on Fluorescence Sensors in Multicomponent Metal-Organic Frameworks for in Vitro Cyanide Detection. *Angew. Chem. Int. Ed.* **2020**, *59*, 9319–9323. [[CrossRef](#)]
24. Shi, P.-F.; Hu, H.-C.; Zhang, Z.-Y.; Xiong, G.; Zhao, B. Heterometal-organic frameworks as highly sensitive and highly selective luminescent probes to detect I⁻ ions in aqueous solutions. *Chem. Commun.* **2015**, *51*, 3985–3988. [[CrossRef](#)]
25. Li, G.; Liu, W.-S.; Yang, S.-L.; Zhang, L.; Bu, R.; Gao, E.-Q. Anion-Afforded Functions of Ionic Metal-Organic Frameworks: Ionochromism, Anion Conduction, and Catalysis. *Inorg. Chem.* **2022**, *61*, 902–910. [[CrossRef](#)]
26. He, H.; Hashemi, I.; Hu, M.-L.; Morsali, A. The role of the counter-ion in metal-organic frameworks' chemistry and applications. *Coord. Chem. Rev.* **2018**, *376*, 319–347. [[CrossRef](#)]
27. Noori, Y.; Akhbari, K. Post-synthetic ion-exchange process in nanoporous metal-organic frameworks; an effective way for modulating their structures and properties. *RSC Adv.* **2017**, *7*, 1782–1808. [[CrossRef](#)]
28. Dybtsev, D.N.; Kovalenko, K.A.; Mironov, Y.V.; Fedin, V.P.; Férey, G.; Yakovleva, N.A.; Berdonosova, E.A.; Klyamkin, S.N.; Kogan, E.V. Reversible sorption of hydrogen on the novel hybrid material based on mesoporous chromium(III) terephthalate with included rhenium clusters. *Russ. Chem. Bull.* **2009**, *58*, 1623–1626. [[CrossRef](#)]
29. Kovalenko, K.A.; Ruban, N.V.; Adonin, S.A.; Korneev, D.V.; Erenburg, S.B.; Trubina, S.V.; Kvashnina, K.; Sokolov, M.N.; Fedin, V.P. Bi(III) immobilization inside MIL-101: Enhanced photocatalytic performance. *New J. Chem.* **2017**, *41*, 2255–2260. [[CrossRef](#)]
30. Noro, S.-I.; Mizutani, J.; Hijikata, Y.; Matsuda, R.; Sato, H.; Kitagawa, S.; Sugimoto, K.; Inubushi, Y.; Kubo, K.; Nakamura, T. Porous coordination polymers with ubiquitous and biocompatible metals and a neutral bridging ligand. *Nat. Commun.* **2015**, *6*, 5851. [[CrossRef](#)] [[PubMed](#)]
31. Huang, Y.-R.; Lin, X.-L.; Chen, B.; Zheng, H.-D.; Chen, Z.-R.; Li, H.-H.; Zheng, S.-T. Thermal-Responsive Polyoxometalate-Metalloviologen Hybrid: Reversible Intermolecular Three-Component Reaction and Temperature-Regulated Resistive Switching Behaviors. *Angew. Chem. Int. Ed.* **2021**, *60*, 16911–16916. [[CrossRef](#)] [[PubMed](#)]

32. Chorazy, S.; Zakrzewski, J.J.; Reczyński, M.; Sieklucka, B. Multi-colour uranyl emission efficiently tuned by hexacyanidometallates within hybrid coordination frameworks. *Chem. Commun.* **2019**, *55*, 3057–3060. [[CrossRef](#)]
33. Zakrzewski, J.J.; Sieklucka, B.; Chorazy, S. Europium(III) Photoluminescence Governed by d^8 – d^{10} Heterometallophilic Interactions in Trimetallic Cyanido-Bridged Coordination Frameworks. *Inorg. Chem.* **2020**, *59*, 1393–1404. [[CrossRef](#)]
34. Wang, D.-H.; Zhao, L.-M.; Lin, X.-Y.; Wang, Y.-K.; Zhang, W.-T.; Song, K.-Y.; Li, H.-H.; Chen, Z.-R. Iodoargentate/iodobismuthate-based materials hybridized with lanthanide-containing metalloviologens: Thermochromic behaviors and photocurrent responses. *Inorg. Chem. Front.* **2018**, *5*, 1162–1173. [[CrossRef](#)]
35. He, Y.; Huang, Y.-R.; Li, Y.-L.; Li, H.-H.; Chen, Z.-R.; Jiang, R. Encapsulating Halometallates into 3-D Lanthanide-Viologen Frameworks: Controllable Emissions, Reversible Thermochromism, Photocurrent Responses, and Electrical Bistability Behaviors. *Inorg. Chem.* **2019**, *58*, 13862–13880. [[CrossRef](#)]
36. Long, D.-L.; Lake, A.J.; Champness, N.R.; Wilson, C.; Schröder, M. Unprecedented Seven- and Eight-Connected Lanthanide Coordination Networks. *Angew. Chem. Int. Ed.* **2001**, *40*, 2443–2447. [[CrossRef](#)]
37. Ma, F.; Sun, R.; Sun, A.-H.; Xiong, J.; Sun, H.-L.; Gao, S. Regulating the structural dimensionality and dynamic properties of a porous dysprosium coordination polymer through solvent molecules. *Inorg. Chem. Front.* **2020**, *7*, 930–938. [[CrossRef](#)]
38. Chen, B.; Huang, Y.-R.; Song, K.-Y.; Lin, X.-L.; Li, H.-H.; Chen, Z.-R. Molecular Nonvolatile Memory Based on $[\alpha\text{-GeW}_{12}\text{O}_{40}]^{4-}$ /Metalloviologen Hybrids Can Work at High Temperature Monitored by Chromism. *Chem. Mater.* **2021**, *33*, 2178–2186. [[CrossRef](#)]
39. Qian, J.-F.; Tian, W.-J.; Yang, S.; Sun, Z.-H.; Chen, L.; Wei, M.-J.; Wu, Z.; He, M.-Y.; Zhang, Z.-H.; Mei, L. Auxiliary Ligand-Dependent Adaptive Regulation of Uranyl Coordination in Mixed-Ligand Uranyl Compounds of Flexible Biphenyltetracarboxylic Acid. *Inorg. Chem.* **2020**, *59*, 17659–17670. [[CrossRef](#)] [[PubMed](#)]
40. Toma, O.; Mercier, N.; Allain, M.; Meinardi, F.; Forni, A.; Botta, C. Mechanochromic Luminescence of N,N' -Dioxide-4,4'-bipyridine Bismuth Coordination Polymers. *Cryst. Growth Des.* **2020**, *20*, 7658–7666. [[CrossRef](#)]
41. Ma, F.; Xiong, J.; Meng, Y.-S.; Yang, J.; Sun, H.-L.; Gao, S. Rational construction of a porous lanthanide coordination polymer featuring reversible guest-dependent magnetic relaxation behavior. *Inorg. Chem. Front.* **2018**, *5*, 2875–2884. [[CrossRef](#)]
42. Hon, P.K.; Mak, T.C.W. Isolation and crystal structures of 1:3 molecular complexes of triethylenediamine- N,N' -dioxide with hydrogen peroxide and water. *J. Crystallogr. Spectrosc. Res.* **1987**, *17*, 419–429. [[CrossRef](#)]
43. Abasheeva, K.D.; Demakov, P.A.; Fedin, V.P. Diverse Hydrogen-Bonded Structural Motifs in 1,4-Diazabicyclo[2.2.2]octane N,N' -Dioxide Salts with Oxoanions. *Molbank* **2022**, *2022*, M1508. [[CrossRef](#)]
44. Sun, F.-X.; Zhu, G.-S.; Fang, Q.-R.; Qiu, S.-L. A novel 3D metal-organic framework with the pcu topology constructed from 1,4-diaza-bicyclo[2.2.2]octane- N,N' -dioxide. *Inorg. Chem. Comm.* **2007**, *10*, 649. [[CrossRef](#)]
45. Demakov, P.A.; Romanov, A.S.; Samsonenko, D.G.; Dybtsev, D.N.; Fedin, V.P. Synthesis and structure of manganese(II) coordination polymers with 1,4-diazabicyclo[2.2.2]octane N,N' -dioxide: Solvent and template effects. *Russ. Chem. Bull.* **2020**, *69*, 1511–1519. [[CrossRef](#)]
46. Abasheeva, K.D.; Demakov, P.A.; Dybtsev, D.N.; Fedin, V.P. Crystal Structure of Coordination Cobalt(II) and Zinc(II) polymers with 1,4-Diazabicyclo[2.2.2]Octane N,N' -Dioxide. *J. Struct. Chem.* **2022**, *63*, 1349–1357. [[CrossRef](#)]
47. Demakov, P.A.; Ovchinnikova, A.A.; Fedin, V.P. SYNTHESIS, structure, and optical properties of the lanthanum(III) cationic coordination polymer with 1,4-Diazabicyclo[2.2.2]Octane N,N' -Dioxide. *J. Struct. Chem.* **2023**, *64*, 199–207. [[CrossRef](#)]
48. Demakov, P.A.; Samsonenko, D.G.; Dybtsev, D.N.; Fedin, V.P. Zinc(II) metal-organic frameworks with 1,4-diazabicyclo[2.2.2]octane N,N' -dioxide: Control of the parameters of the cationic porous framework and optical properties. *Russ. Chem. Bull.* **2022**, *71*, 83–90. [[CrossRef](#)]
49. Demakov, P.A.; Yudina, Y.A.; Samsonenko, D.G.; Dybtsev, D.N.; Fedin, V.P. Crystal structure of zinc coordination polymers based on 1,4-diazabicyclo[2.2.2]octane N,N' -dioxide: Effect of hydrophobicity of carboxylate ligands. *J. Struct. Chem.* **2021**, *62*, 403–411. [[CrossRef](#)]
50. Chen, L.Z.; Sun, J. Reversible ferroelectric phase transition of 1,4-diazabicyclo[2,2,2]octane N,N' -dioxide di(perchlorate). *Inorg. Chem. Comm.* **2017**, *76*, 67–70. [[CrossRef](#)]
51. Ye, H.-Y.; Zhang, Y.; Noro, S.-I.; Kubo, K.; Yoshitake, M.; Liu, Z.-Q.; Cai, H.-L.; Fu, D.-W.; Yoshikawa, H.; Awaga, K.; et al. Molecule-displacive ferroelectricity in organic supramolecular solids. *Sci. Rep.* **2013**, *3*, 2249. [[CrossRef](#)]
52. Chen, L.; Ji, Q.; Wang, X.; Pan, Q.; Cao, X.; Xu, G. Two novel metal-organic coordination polymers based on ligand 1,4-diazabicyclo[2.2.2]octane N,N' -dioxide with phase transition, and ferroelectric and dielectric properties. *CrystEngComm* **2017**, *19*, 5907–5914. [[CrossRef](#)]
53. Yang, Y.-C.; Wu, R.; Cai, Y.; Zhou, Z.-H. Unusual N-oxide formation in the peroxidation of cobalt(II) ethylenediaminetetraacetates. *Dalton Trans.* **2017**, *46*, 1290–1296. [[CrossRef](#)]
54. Liu, X.; Feng, X.; Meihaus, K.R.; Meng, X.; Zhang, Y.; Li, L.; Liu, J.-L.; Pedersen, K.S.; Keller, L.; Shi, W.; et al. Coercive Fields Above 6 T in Two Cobalt(II)-Radical Chain Compounds. *Angew. Chem. Int. Ed.* **2020**, *59*, 10610–10618. [[CrossRef](#)] [[PubMed](#)]
55. Ovcharenko, V.; Kuznetsova, O.; Fursova, E.; Letyagin, G.; Romanenko, G.; Bogomyakov, A.; Zueva, E. Simultaneous Introduction of Two Nitroxides in the Reaction: A New Approach to the Synthesis of Heterospin Complexes. *Inorg. Chem.* **2017**, *56*, 14567–14576. [[CrossRef](#)] [[PubMed](#)]
56. Lin, X.; Pu, M.; Sang, X.; Li, S.; Liu, X.; Wu, Y.-D.; Feng, X. Asymmetric Catalytic (2+1) Cycloaddition of Thioketones to Synthesize Tetrasubstituted Thiiranes. *Angew. Chem. Int. Ed.* **2022**, *61*, e202201151. [[CrossRef](#)]

57. Belov, A.S.; Vologzhanina, A.V.; Fedorov, Y.V.; Kuznetsov, E.V.; Voloshin, Y.Z. Unexpected transformation of mono- to bis-macrocyclic dimethylglyoximate framework in a chloroform solution: Photochemical, MALDI-TOF MS and X-ray diffraction studies. *Inorg. Chem. Commun.* **2013**, *35*, 242–246. [[CrossRef](#)]
58. Ran, J.-W.; Tong, Y.-P. Crystal Structures, Magnetic Properties, and Theoretical Investigations of Three Linear Cluster Complexes with Pyridine-2-Amidoxime. *J. Struct. Chem.* **2018**, *59*, 1433–1439. [[CrossRef](#)]
59. Sniekers, J.; Geysens, P.; Vander Hoogerstraete, T.; Van Meervelt, L.; Fransaeer, J.; Binnemans, K. Cobalt(ii) liquid metal salts for high current density electrodeposition of cobalt. *Dalton Trans.* **2018**, *47*, 4975–4986. [[CrossRef](#)]
60. Yin, X.-J.; Zhu, L.-G. Structural variation from trinuclears to 1D chains: Syntheses, structures and properties. *Appl. Organomet. Chem.* **2019**, *33*, e4796. [[CrossRef](#)]
61. Desiraju, G.R. C–H...O and other weak hydrogen bonds. From crystal engineering to virtual screening. *Chem. Commun.* **2005**, *2005*, 2995–3001. [[CrossRef](#)] [[PubMed](#)]
62. Zavras, A.; Fry, J.A.; Beavers, C.M.; Talbo, G.H.; Richards, A.F. 2-Pyridylmethylphosphonic acid: A flexible, multi-dentate ligand for metal phosphonates. *CrystEngComm* **2011**, *13*, 3551–3561. [[CrossRef](#)]
63. Goodgame, D.M.L.; Menzer, S.; Smith, A.M.; Williams, D.J. Formation of a novel three-dimensional network of 48-membered rings in the compound $[\text{Ni}(m\text{-XBP})_3](\text{ClO}_4)_2$. *J. Chem. Soc. Chem. Commun.* **1994**, *1994*, 1825–1826. [[CrossRef](#)]
64. Pal Singh Pannu, A.; Kapoor, P.; Hundal, G.; Kapoor, R.; Martinez-Ripoll, M.; Singh Hundal, M. A self assembled 3-D network propagated by coordination polymerization and H-bonding: Synthesis and X-ray crystal structure of $[\{\text{Co}(\text{L})_2(\text{H}_2\text{O})_2\}(\text{ClO}_4)_2(\text{CH}_3\text{COCH}_3)_2(\text{H}_2\text{O})_2]_n$, where L = N,N-diisopropylisonicotinamide. *J. Coord. Chem.* **2011**, *64*, 1566–1577. [[CrossRef](#)]
65. Shi, J.-M.; Zhang, E.-X.; Wu, C.-J.; Yi, L.; Ma, J.-P. Synthesis, crystal structure and magnetism study on a three-dimensional Co(II) coordination polymer with 2,5-dimethylpyrazine-1,4-dioxide as bridging ligand. *J. Coord. Chem.* **2007**, *60*, 1667–1672. [[CrossRef](#)]
66. Zhang, L.-P.; Du, M.; Lu, W.-J.; Mak, T.C.W. Anion-controlled formation of diverse porous cobalt(II) coordination polymers with 1,2-bis(4-pyridyl)ethane- N,N' -dioxide. *Inorg. Chem. Commun.* **2005**, *8*, 623–625. [[CrossRef](#)]
67. Zhou, G.X.; Wang, X.Y.; Yan, G.; Liao, G.Y.; Xia, H. Syntheses, crystal structures, and properties of various one-dimensional coordination polymers based on macrocyclic metallic tectons and dicarboxylic acid ligand. *Russ. J. Coord. Chem.* **2016**, *42*, 461–469. [[CrossRef](#)]
68. Su, Z.; Bai, Z.-S.; Xu, J.; Okamura, T.; Liu, G.-X.; Chu, Q.; Wang, X.-F.; Sun, W.-Y.; Ueyama, N. Synthesis, structure and property of cobalt(II) complexes with 3,5-di(1H-imidazol-1-yl)benzoic acid. *CrystEngComm* **2009**, *11*, 873–880. [[CrossRef](#)]
69. Wang, Q.; Ou, G.-C. Crystal structure of *catena*-poly $[(5,5,7,12,12,14\text{-hexamethyl-1,4,8,11-tetraazacyclotetradecane-}\kappa^4N,N',N'',N''')$ nickel(II)- $(\mu_2\text{-perchlorato-}\kappa^2O:O')$] 3,5-dicarboxybenzoate—Methanol (1/2), $\text{C}_{27}\text{H}_{49}\text{ClN}_4\text{NiO}_{12}$. *Z. Krist. New Cryst St.* **2022**, *237*, 745–747. [[CrossRef](#)]
70. Xu, Z.; Bai, Z.; Sun, W. Synthesis and Crystal Structure of an Unprecedented Supramolecular Complex $[\text{Co}(\mu_2\text{-ClO}_4)_2(\text{H}_2\text{O})_2] \cdot 2\text{MA}$. *Chin. J. Chem.* **2009**, *27*, 501–504. [[CrossRef](#)]
71. Spek, A.L. Single-crystal structure validation with the program PLATON. *J. Appl. Crystallogr.* **2003**, *36*, 7–13. [[CrossRef](#)]
72. Kumar Maity, D.; Dey, A.; Ghosh, S.; Halder, A.; Pratim Ray, P.; Ghoshal, D. Set of Multifunctional Azo Functionalized Semiconducting Cd(II)-MOFs Showing Photoswitching Property and Selective CO_2 Adsorption. *Inorg. Chem.* **2018**, *57*, 251–263. [[CrossRef](#)] [[PubMed](#)]
73. Schneemann, A.; Bon, V.; Schwedler, I.; Senkovska, I.; Kaskel, S.; Fischer, R.A. Flexible Metal–Organic Frameworks. *Chem. Soc. Rev.* **2014**, *43*, 6062–6096. [[CrossRef](#)] [[PubMed](#)]
74. Férey, G.; Serre, C. Large Breathing Effects in Three-Dimensional Porous Hybrid Matter: Facts, Analyses, Rules and Consequences. *Chem. Soc. Rev.* **2009**, *38*, 1380. [[CrossRef](#)] [[PubMed](#)]
75. Husna, A.; Hossain, I.; Jeong, I.; Kim, T.-H. Mixed Matrix Membranes for Efficient CO_2 Separation Using an Engineered UiO-66 MOF in a Pebax Polymer. *Polymers* **2022**, *14*, 655. [[CrossRef](#)]
76. Demakov, P.A.; Volynkin, S.S.; Samsonenko, D.G.; Fedin, V.P.; Dybtsev, D.N. A Selenophene-Incorporated Metal–Organic Framework for Enhanced CO_2 Uptake and Adsorption Selectivity. *Molecules* **2020**, *25*, 4396. [[CrossRef](#)]
77. Li, Z.; Ma, X.; Xiong, S.; Ye, Y.; Yao, Z.; Lin, Q.; Zhang, Z.; Xiang, S. Facile synthesis of oxidized activated carbons for high-selectivity and low-enthalpy CO_2 capture from flue gas. *New J. Chem.* **2018**, *42*, 4495–4500. [[CrossRef](#)]
78. Lukyanova, M.B.; Tkachev, V.V.; Lukyanov, B.S.; Pugachev, A.D.; Ozhogin, I.V.; Komissarova, O.A.; Aldoshin, S.M.; Minkin, V.I. Structure Investigation of New Condensation Products of 1,2,3,3-Tetramethylindolenium with Methoxy-substituted Diformylphenols. *J. Struct. Chem.* **2018**, *59*, 565–570. [[CrossRef](#)]
79. Jian, Y.-F.; Fu, B.; Fu, S.; Liu, X. Synthesis, Crystal Structure, and Photoluminescence of a Lithium Perchlorate Complex with 18-Crown-6. *J. Struct. Chem.* **2019**, *60*, 1119–1125. [[CrossRef](#)]
80. Zanjanchi, M.A.; Tabatabaeian, K.; Hosseinzadeh, F. Contribution of Diffuse Reflectance Spectroscopy to Monitoring the Synthesis Improvement of Encapsulated Complexes. *Russ. J. Coord. Chem.* **2005**, *31*, 585–587. [[CrossRef](#)]
81. Kashif, M.K.; Milhuisen, R.A.; Nippe, M.; Hellerstedt, J.; Zee, D.Z.; Duffy, N.W.; Halstead, B.; De Angelis, F.; Fantacci, S.; Fuhrer, M.S.; et al. Cobalt Polypyridyl Complexes as Transparent Solution-Processable Solid-State Charge Transport Materials. *Adv. Energy Mat.* **2016**, *6*, 1600874. [[CrossRef](#)]
82. Jbali, W.; Selmi, W.; Jouffret, L.; Marzouki, R.; Zid, M.F. Synthesis, crystal structure, spectroscopic study and Hirshfeld surface analysis of $[\text{Ni}(\text{C}_6\text{H}_8\text{N}_2)_3]\text{Cl}_2 \cdot 2(\text{H}_2\text{O})$. *J. Mol. Struct.* **2021**, *1225*, 129123. [[CrossRef](#)]

83. Bhattacharjee, S.; Matin, M.A.; Akhter Simol, H.; Hosen, A. Environmentally Friendly Room Temperature Synthesis of 1-Tetralone over Layered Double Hydroxide-Hosted Sulphonato-Salen-Nickel(II) Complex. *Green Sustain. Chem.* **2023**, *13*, 9–22. [[CrossRef](#)]
84. Demakov, P.A.; Bogomyakov, A.S.; Urlukov, A.S.; Andreeva, A.Y.; Samsonenko, D.G.; Dybtsev, D.N.; Fedin, V.P. Transition Metal Coordination Polymers with Trans-1,4-Cyclohexanedicarboxylate: Acidity-Controlled Synthesis, Structures and Properties. *Materials* **2020**, *13*, 486. [[CrossRef](#)] [[PubMed](#)]
85. Boča, R. Zero-field splitting in metal complexes. *Coord. Chem. Rev.* **2004**, *248*, 757–815. [[CrossRef](#)]
86. Dubskikh, V.A.; Lysova, A.A.; Samsonenko, D.G.; Lavrov, A.N.; Dybtsev, D.N.; Fedin, V.P. Coordination Polymers of Ni(II) with Thiophene Ligands: Synthesis, Structures, and Magnetic Properties. *Russ. J. Coord. Chem.* **2021**, *47*, 664–669. [[CrossRef](#)]
87. *CrysAlisPro 1.171.38.46*; Rigaku Oxford Diffraction: The Woodlands, TX, USA, 2015.
88. Sheldrick, G.M. SHELXT—Integrated space-group and crystal-structure determination. *Acta Crystallogr.* **2015**, *A71*, 3–8. [[CrossRef](#)]
89. Sheldrick, G.M. Crystal structure refinement with SHELXL. *Acta Crystallogr.* **2015**, *C71*, 3–8. [[CrossRef](#)]

Disclaimer/Publisher’s Note: The statements, opinions and data contained in all publications are solely those of the individual author(s) and contributor(s) and not of MDPI and/or the editor(s). MDPI and/or the editor(s) disclaim responsibility for any injury to people or property resulting from any ideas, methods, instructions or products referred to in the content.